PCCP

PAPER

View Article Online
View Journal | View Issue

Cite this: *Phys. Chem. Chem. Phys.*, 2019, **21**, 11455

Gas sensing properties of buckled bismuthene predicted by first-principles calculations†

Wenfeng Pan,[a] Ning Qi,*[a] Bin Zhao,[b] Sheng Chang,[a] Shizhuo Ye [a] and Zhiquan Chen *[a]

Received 28th February 2019,
Accepted 7th May 2019

DOI: 10.1039/c9cp01174a

rsc.li/pccp

First-principles calculations are used to study the structural, electronic, transport and optical properties of buckled bismuthene with the adsorption of various gas molecules such as CO, O_2, H_2O, NH_3, SO_2, NO and NO_2. By considering the van der Waals interactions between the gas molecules and buckled bismuthene, we find that the buckled bismuthene shows superior gas sensing performance to other 2D materials such as graphene and MoS_2. The adsorption of CO, O_2, H_2O and NH_3 molecules is physisorption, whereas SO_2, NO and NO_2 are chemisorbed on the buckled bismuthene with large charge transfer and strong adsorption energy. After adsorption, charges are transferred from buckled bismuthene to the molecules and the quantum conductance is changed by the adsorbed molecules. Furthermore, the work function of buckled bismuthene is changed with the adsorption of different molecules. Our results show that the electronic, transport and optical properties of buckled bismuthene are sensitive to the adsorption of gas molecules, which suggests that buckled bismuthene holds great potential for application in gas sensors.

1 Introduction

Recently, gas sensing has received great attention because of its widespread application in the fields of industrial control, medical applications, indoor air quality supervision and environment pollution monitoring. Motivated by the increasing demand for highly sensitive, selective, stable, reversible and portable gas sensors, researchers started exploring new sensing materials.[1–5] Among them two-dimensional (2D) materials have attracted great interest because of their high electrical conductivities, low electrical noise and large surface-to-volume ratio.[6] Following the extensive studies of graphene, other 2D materials such as MoS_2,[7,8] germanene,[9,10] stanene[11–13] and arsenene[14,15] also have received much attention, since they show a much stronger adsorption of gas molecules than graphene due to their buckled structure originating from the sp^3 hybridization.[16] However, there is still great demand for the search for new suitable 2D adsorbent materials with buckled structure.

Freestanding single-layer bismuth, named bismuthene, possesses different structures such as buckled honeycomb (b-Bi), symmetric washboard (w-Bi) and asymmetric washboard (aw-Bi) structures, and they are predicted to be dynamically and thermally stable based on theoretical calculations.[17] Among these structures, buckled bismuthene (b-Bi) with a honeycomb-like structure similar to the single bilayer (BL) Bi(111) structure is the most stable phase and it possesses a relatively high carrier mobility (several thousands of $cm^2\ V^{-1}\ s^{-1}$)[18] compared to other typical 2D materials like MoS_2 (around 200 $cm^2\ V^{-1}\ s^{-1}$).[19] Encouragingly, BL Bi(111) film has been successfully grown on Bi_2Te_3[20] and SiC[21] substrates. Theoretical calculations predicted that BL Bi(111) is an elemental topological insulator as a function of strain and perpendicular electric field.[22–24] Moreover, b-Bi manifested enhanced thermoelectric properties at an appropriate operating temperature.[25] Very recently, the effects of different atoms and molecules on b-Bi have been discussed theoretically,[26–28] showing a modification of electronic properties similar to that in other materials.[29–31] But until now, a systematic study of the influence of gas adsorption on b-Bi is still absent.

In this work, we systematically studied the adsorption behaviors of various gas molecules (CO, O_2, H_2O, NH_3, SO_2, NO, and NO_2) on b-Bi using first-principles calculations. The most stable structures, adsorption energy, charge transfer and electronic structures after adsorption of gas molecules are discussed. Our results reveal that CO, O_2, H_2O and NH_3 exhibit relatively weak interactions with b-Bi, while SO_2, NO and NO_2 adhere well on b-Bi with higher adsorption energy and more

[a] *Hubei Nuclear Solid Physics Key Laboratory, Department of Physics, Wuhan University, Wuhan 430072, China. E-mail: ningqi@whu.edu.cn, chenzq@whu.edu.cn*

[b] *State College of Science, Zhongyuan University of Technology, Zhengzhou 450007, China*

† Electronic supplementary information (ESI) available: Total (DOS) and partial (PDOS) density of states of pristine b-Bi and gas on b-Bi (with SOC), *I–V* curves of pristine b-Bi and NH_3 on b-Bi, and the diffusion energy barrier of gas on b-Bi. See DOI: 10.1039/c9cp01174a

charge transfer. In addition, the quantum conductance and the work function of b-Bi vary with the adsorption of different gas molecules, which indicates that the transport and optical properties of b-Bi can be tuned by selective adsorption of gas molecules.

2 Methods

First-principles calculations are carried out based on density functional theory (DFT) with projector-augmented wave (PAW) pseudopotentials, as implemented in the Vienna ab initio simulation package (VASP).[32–34] The exchange correlation interaction is described by the generalized gradient approximation (GGA) with the Perdew, Burke and Ernzerhof (PBE) functional.[35] The van der Waals (vdW) effects are included using the D2-Grimme correction (DFT-D2) to obtain a better description of long-range vdW interactions between b-Bi and gas molecules.[36] The kinetic energy cutoff for the plane wave expansion is set to be 500 eV. A $4 \times 4 \times 1$ supercell is employed in the simulated system with an empty space in the z direction larger than 15 Å to avoid interaction with neighboring supercells. The Monkhorst–Pack k-points in the Brillouin zone are set as $3 \times 3 \times 1$ for geometry optimization and $5 \times 5 \times 1$ for electronic property calculations. In all calculations, the convergence criterion for the energy between two successive iterations is chosen as 10^{-5} eV and the maximum force on each atom upon structure optimization is less than 0.02 eV Å^{-1}. Spin–orbit coupling (SOC) is considered to see its influence on the electronic structures of the systems and climbing image nudged elastic band (CI-NEB)[37,38] is used to investigate the diffusion behavior of some gas molecules on b-Bi.

To evaluate the adsorption stability of gas molecules on b-Bi, the adsorption energy is defined as:

$$E_{ad} = E_{b\text{-}Bi/gas} - E_{b\text{-}Bi} - E_{gas}, \quad (1)$$

where $E_{b\text{-}Bi/gas}$ represents the total energy of the adsorbed gas b-Bi system, and $E_{b\text{-}Bi}$ and E_{gas} represent the total energy of pristine b-Bi and the free gas molecule, respectively. According to the definition, a more negative value of E_{ad} suggests that the adsorption is stronger. Bader analysis is used to obtain the charge transfer from b-Bi to gas molecules.[39] To visualize the charge redistribution between gas molecules and b-Bi, we calculated the charge density difference (CDD) by subtracting the charge density of the free gas molecule (ρ_{gas}) and the pristine b-Bi ($\rho_{b\text{-}Bi}$) from the total charge density of adsorbed gas b-Bi ($\rho_{b\text{-}Bi/gas}$) as follows:

$$\Delta\rho = \rho_{b\text{-}Bi/gas} - \rho_{b\text{-}Bi} - \rho_{gas}, \quad (2)$$

where $\rho_{b\text{-}Bi}$ and ρ_{gas} are calculated with each component at the same positions as in the b-Bi/gas configuration.

For the calculation of electron transport properties, we use DFT methods combined with the nonequilibrium Green's function (NEGF) formalism as implemented in the Atomistix Toolkit (ATK) package.[40] The exchange correlation functional is described by GGA-PBE and the electron wave function is expanded using a double-zeta polarized (DZP) basis set. The plane-wave cutoff energy is 150 Ry and k-point sampling of $1 \times 1 \times 100$ is adopted. The conductance is calculated by the transmission coefficient $T(\varepsilon)$ at the Fermi level:

$$C(\varepsilon) = G_0 T(\varepsilon) \quad (3)$$

where $G_0 = 2e^2/h$ is the quantum unit of conductance, e is the charge of an electron and h is Planck's constant.

3 Results and discussion

The top and side views of the optimized b-Bi supercell ($4 \times 4 \times 1$) are displayed in Fig. 1. The calculated lattice constants of the pristine b-Bi are $a = b = 4.34$ Å, which are 0.2 Å smaller than those of the experimental value of a 3D Bi crystal.[41] The buckling parameter Δ is 1.73 Å, and the Bi–Bi bond length is 3.05 Å. The band structures depicted in Fig. 1(c) suggest that b-Bi has a direct band gap of 0.55 eV at the Γ point without the inclusion of SOC, while it has an indirect band gap of 0.50 eV with the valence band maximum (VBM) shifting away from the Γ point and the conducting band minimum (CBM) still located at the Γ point in the presence of SOC, which are consistent with previous studies.[17,24,25,42] To acquire the most stable adsorption configuration, we considered several structures with the molecules being aligned in a tilted, parallel or perpendicular direction to the b-Bi surface in the four possible adsorption sites (Fig. 1(a)), including the top site above the center of a hexagon (H), the bridge of a Bi–Bi bond (B), and on top of an upper Bi atom (T) and a lower Bi atom (V). Meanwhile, we also carried out the geometric optimization of free gas molecules. The results show that the bond lengths are 1.021, 1.143, 1.233, 0.970, 1.448, 1.170, and 1.212 Å for NH_3, CO, O_2, H_2O, SO_2, NO, and NO_2, respectively. The bond angles of H_2O, NH_3, SO_2, and NO_2 are 104.5°, 106.4°, 119.3°, and 133.8°, respectively. All of these molecular structure data correspond with previous theoretical and experimental reports.[8,43,44] The gas molecule adsorption parameters of the most stable adsorption configurations are summarized in Table 1. By comparing with the adsorption energy and charge transfer of these molecules in graphene[45–47] and MoS_2,[8,48] we find that b-Bi has a much higher adsorption energy and larger charge transfer leading to a stronger change of

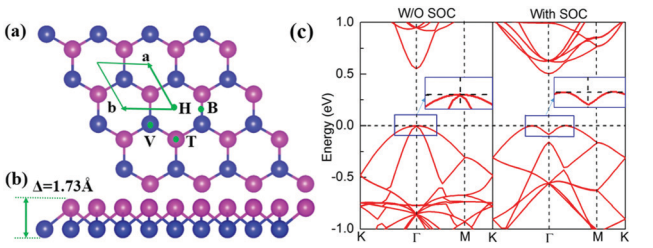

Fig. 1 The top (a) and side (b) views of the b-Bi supercell ($4 \times 4 \times 1$), the four possible adsorption sites H, B, T and V are labeled. The fuchsia and blue spheres denote the bismuth atoms in the upper and lower layer, respectively. (c) Band structures of pristine b-Bi without (left panels) and with (right panels) SOC, the Fermi level is set to zero and indicated by the black dashed line.

Table 1 Calculation results of gas molecule adsorption on b-Bi: the adsorption energy E_{ad}, the charge transfer from b-Bi to molecules ΔQ, and the shortest distance from the adsorbed molecules to the host Bi atom of b-Bi $d_{x\text{-}Bi}$

Gas molecule	E_{ad} (eV)	ΔQ (e)	$d_{x\text{-}Bi}$ (Å)
CO	−0.177	0.096	3.486
O_2	−0.221	0.236	3.335
H_2O	−0.270	0.064	2.953
NH_3	−0.284	0.019	3.194
SO_2	−0.398	0.329	3.205
NO	−0.416	0.344	2.773
NO_2	−0.811	0.663	2.737

resistivity, which makes b-Bi advantageous over graphene and MoS_2 for use as a gas sensor.

3.1 CO adsorption

For CO adsorption, the strongest binding structure is plotted in Fig. 2(a). The molecule is located above the V site with the C atom pointing towards the surface and the C–O bond aligned almost vertical to the b-Bi slab. After adsorption, the C–O bond is elongated to 1.148 Å, the nearest distance between the surface Bi atom and the C atom is 3.486 Å, which is larger than the sum of the covalent radii of Bi and C atoms (2.26 Å),[49] and the adsorption energy for this structure is −0.177 eV, which suggests the physisorption behavior of CO molecules on b-Bi similar to the case of CO adsorption on antimonene,[50] phosphorene,[51] and germanene.[10]

To gain a deeper insight into the electronic interaction of CO and b-Bi, we calculated the charge density difference (CDD), which is plotted in Fig. 2(b). It can be seen that the charges are accumulated on the O atom, while charge depletion appears on the C–O bond and the empty space between the b-Bi and the CO molecule, which reveals that the charges are transferred from b-Bi to the CO molecule. Bader charge analysis quantifies the amount of transferred charges and it reveals that the CO molecule obtains 0.096 e from b-Bi, acting as a weak electron acceptor. From the band structure without SOC shown in Fig. 2(c), one can see that the band structure is changed slightly with an enlarged direct band gap of 0.57 eV compared with that of the pristine b-Bi. However, when SOC is included, the band structure has an indirect band gap of 0.47 eV and shows Rashba splitting. The calculated total and partial DOS are shown in Fig. 2(d) and Fig. S1(b) (ESI†). The contribution of CO to the total DOS is localized between 0.5 and 3.0 eV in the conduction bands and around −5.5 eV in the valence bands, which is far from the Fermi level regardless of whether SOC effects are considered. These further confirm that the interaction between CO and b-Bi is physisorption.

3.2 O_2 adsorption

In the case of O_2 adsorption, the most energetically stable structure is plotted in Fig. 3(a), where the O_2 molecule adopts an adsorption structure similar to that of the CO molecule with the O atom located above the lower Bi atom. The bond length of O_2 after adsorption is 1.255 Å, which is slightly longer than that of the free O_2 molecule. From Table 1, we can find that the minimum distance between the O and the Bi atom is 3.335 Å, whereas the Bi–O bond length is 2.14 Å[49] and the value of the adsorption energy is −0.221 eV, revealing that O_2 is also physically adsorbed on the b-Bi sheet.

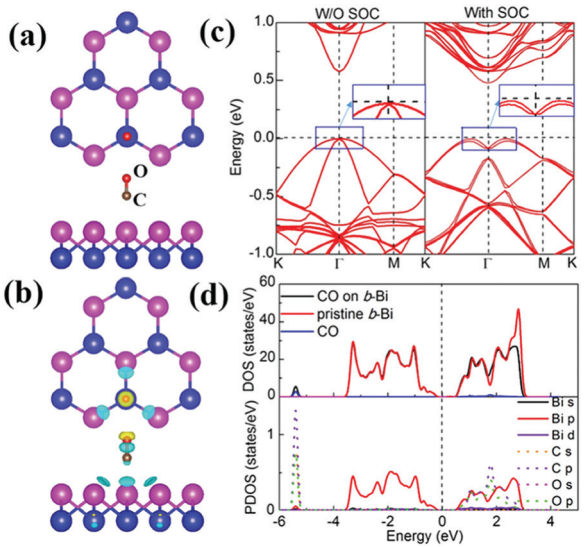

Fig. 2 CO adsorbed on b-Bi. (a) The most stable adsorption structure (top and side view). (b) Charge density difference with an isosurface value of 0.002 e Bohr^{-3}. The yellow and blue regions denote charge accumulation and depletion, respectively. (c) Band structures of b-Bi with CO adsorption (without and with SOC), and (d) the total (DOS) and partial (PDOS) electronic density of states (without SOC). The Fermi level is set to zero and indicated by the black dashed line.

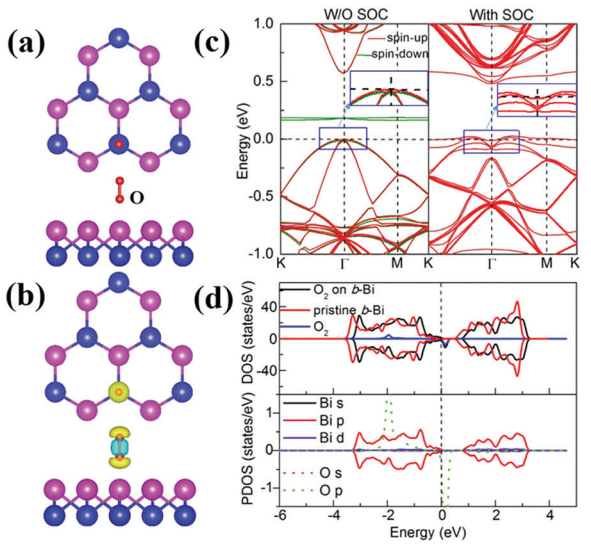

Fig. 3 O_2 adsorbed on b-Bi. (a) The most stable adsorption structure (top and side view). (b) Charge density difference with an isosurface value of 0.005 e Bohr^{-3}. The yellow and blue regions denote charge accumulation and depletion, respectively. (c) Band structures of b-Bi with O_2 adsorption (without and with SOC) and the spin-up and spin-down bands labeled by the red and green lines, respectively. (d) The total (DOS) and partial (PDOS) electronic density of states (without SOC). The Fermi level is set to zero and indicated by the black dashed line.

The CDD for the O_2 adsorption configuration is presented in Fig. 3(b). It is found that charge accumulation appears on the O atoms while charge depletion emerges on the bond of the O_2 molecule. The calculation result of Bader charge analysis indicates that the O_2 molecule obtains 0.236 *e* from b-Bi and acts as a relatively stronger electron acceptor compared with the CO molecule. The band structure analysis after adsorption is presented in Fig. 3(c). In the absence of SOC, the CBM and VBM shift along the direction of increasing energy and an impurity state is introduced in the band gap which induces a magnetic moment of about 1.89 μ_B in b-Bi. The band gap shows a slight increase from 0.55 eV of the pristine sheet to 0.57 eV without considering the impurity state. When SOC is included, the system is not spin-polarized[26] and the Fermi level shifts to the valence band leading to a transition from a semiconductor to a metal. From the PDOS shown in Fig. 3(d) and Fig. S1(C) (ESI†), the impurity state results from the O p orbital of the adsorbed O_2 molecule and there is no obvious orbital hybridization in the O_2/b-Bi structure, further confirming the physisorption of O_2 on b-Bi.

3.3 H_2O adsorption

For H_2O adsorption, the most stable structure is given in Fig. 4(a), where the O–H bonds point toward the surface and the O atom is located above the center of the hexagon. After adsorption, the O–H bond is stretched to 0.977 Å and the H–O–H angle is decreased to 104.1°. The nearest distance between the H_2O molecule and surface Bi atoms is 2.953 Å, which is much longer than the Bi–H bond length of 1.83 Å.[49] The adsorption energy for H_2O is −0.27 eV, indicating the physisorption of the H_2O molecule on b-Bi.

The CDD for H_2O adsorption is presented in Fig. 4(b), where charge accumulation appears on the O atom and the underlying Bi atoms and charge depletion emerges on the O–H bond and the top Bi atom. According to the Bader charge analysis, the H_2O molecule accepts 0.064 e from b-Bi and acts as an electron acceptor. Furthermore, the band structures for H_2O adsorption without and with SOC are presented in Fig. 4(c). We can find that there are minor changes near the Fermi level compared with that of the pristine b-Bi. In addition, the PDOS in Fig. 4(d) and Fig. S1(d) (ESI†) show that a few orbitals of H_2O hybridize with those of Bi atoms in the energy range of −4 to −3 eV, which is far from the Fermi level, further suggesting that the interaction between b-Bi and H_2O is weak, similar to those of the H_2O molecule on phosphorene[51] and antimonene,[52] but is stronger than H_2O adsorption on graphene.[45]

3.4 NH_3 adsorption

Fig. 5(a) shows the most stable structure for NH_3 molecule adsorption on b-Bi. The NH_3 molecule is located at the center of the hexagon with the N atom and the H atoms pointing toward and away from the surface, respectively. The nearest distance between a H atom and Bi atom is 3.194 Å. A similar adsorption structure is found in the cases of NH_3 adsorption on antimonene[52] and a MoS_2 monolayer.[48] The N–H bond length and the H–N–H bond angle after adsorption are 1.023 Å and 107.4°, respectively, which are close to the values of the free NH_3 molecule. From Table 1, we can see that the adsorption energy for NH_3 is −0.284 eV, which is similar to that of H_2O adsorption.

The CDD plotted in Fig. 5(b) depicts the charge redistribution of b-Bi upon NH_3 adsorption, which shows an accumulation of charges on the N atom and a depletion of charges in the vicinity of the b-Bi surface. The NH_3 molecule obtains 0.019 *e* from b-Bi according to the Bader charge analysis. Compared

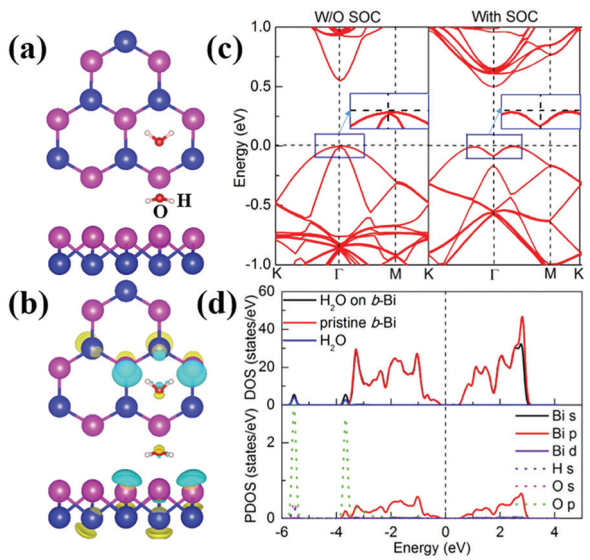

Fig. 4 H_2O adsorbed on b-Bi. (a) The most stable adsorption structure (top and side view). (b) Charge density difference with an isosurface value of 0.005 e Bohr^{-3}. (c) Band structures of b-Bi with H_2O adsorption (without and with SOC), and (d) the total (DOS) and partial (PDOS) electronic density of states (without SOC).

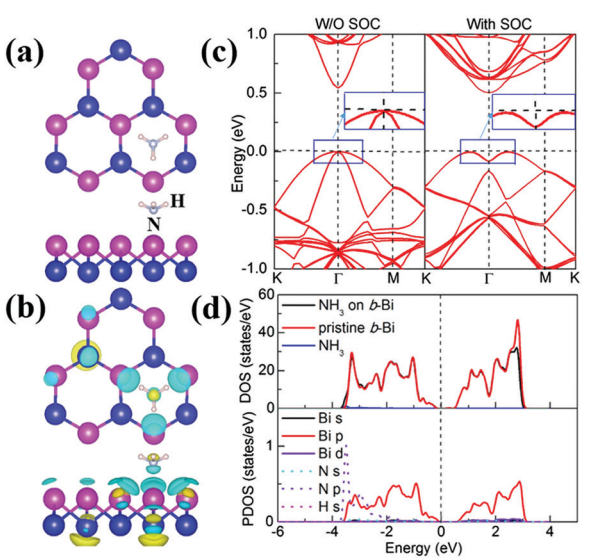

Fig. 5 NH_3 adsorbed on b-Bi. (a) The most stable adsorption structure (top and side view). (b) Charge density difference with an isosurface value of 0.005 e Bohr^{-3}. (c) Band structures of b-Bi with NH_3 adsorption (without and with SOC), and (d) the total (DOS) and partial (PDOS) electronic density of states (without SOC).

with the band of pure b-Bi, the band structures of adsorbed NH_3 b-Bi are almost unchanged and the band gaps are still 0.55 eV and 0.50 eV without and with SOC, respectively. Besides, the DOS of NH_3 on b-Bi shown in Fig. 5(d) and Fig. S1(e) (ESI†) are analogous to that of the pristine b-Bi and the contributions of NH_3 to the DOS are located in the valence band around −3.5 eV, which is far away from the Fermi level, corresponding to a weak interaction between NH_3 and b-Bi.

3.5 SO_2 adsorption

Regarding the adsorption of the SO_2 molecule, the most stable structure is shown in Fig. 6(a), where the two O atoms point away from the surface and the S atom sits above the H site pointing toward the surface. The S–O–S angle after adsorption is reduced from 119.3° of the free gas molecule to 117.6° and the S–O bond length is enlarged to 1.466 Å. Compared with CO, O_2, H_2O and NH_3, the adsorption of SO_2 gives a higher E_a of −0.398 eV indicating a stronger interaction with b-Bi. The nearest distance between S and Bi is calculated to be 3.205 Å, which is larger than the S–Bi bond length, implying the interaction between SO_2 and b-Bi is not a covalent bond. Also, we calculated the electron localization function (ELF) as shown in Fig. 7 to give a description of the electron delocalization or localization between the gas molecule and b-Bi. ELF values of 1.00, 0.50, and 0.00 correspond to fully localized electrons, fully delocalized electrons and very low charge density, respectively. As shown in Fig. 7(a), the ELF value in the interlayer regions of the adsorbed SO_2 system is about 0.13, which manifests that the electrons are delocalized and this reflects an ionic bond between the SO_2 and b-Bi.[50,53,54]

Owing to the relatively strong interaction, the charges around SO_2 are distinctly redistributed as shown in Fig. 6(b).

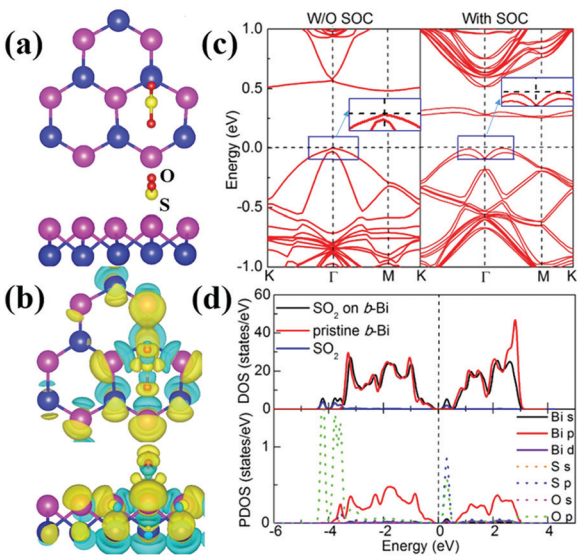

Fig. 6 SO_2 adsorbed on b-Bi. (a) The most stable adsorption structure (top and side view). (b) Charge density difference with an isosurface value of 0.005 e $Bohr^{-3}$. (c) Band structures of b-Bi with SO_2 adsorption (without and with SOC), and (d) the total (DOS) and partial (PDOS) electronic density of states (without SOC).

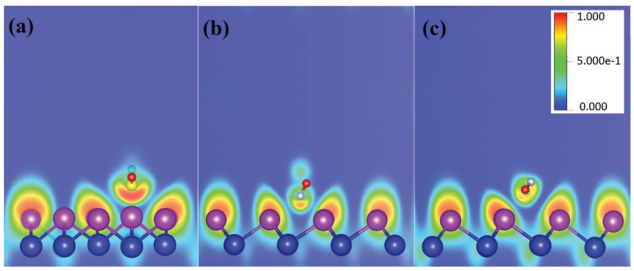

Fig. 7 Electron localization function (ELF) of (a) SO_2, (b) NO and (c) NO_2 adsorbed on b-Bi. The reference bar for the ELF value is provided at the right side.

Charges are accumulated on the SO_2 molecules with a slight depletion on the S–O bond, which is consistent with the enlarged S–O bond length. Charge accumulation and depletion also occur on the Bi atoms near the SO_2 molecule. Bader charge calculations indicate that the SO_2 molecule receives 0.329 *e* from b-Bi, acting as an electron acceptor. The band structures are shown in Fig. 6(c). Similar to the case of O_2 adsorption, there are unoccupied states around 0.5 eV (without SOC) and 0.3 eV (with SOC). The band gaps are 0.58 eV (without SOC) and 0.51 eV (with SOC) without considering the impurity states. The LDOS presented in Fig. 6(d) and Fig. S1(f) (ESI†) suggest that the unoccupied states arise from the overlap between the orbitals of the Bi atom and the p orbitals of the S and O atoms of the SO_2 molecule, which indicates orbital hybridization and confirms the stronger adsorption energy of SO_2 on b-Bi.

3.6 NO adsorption

The most stable structure of NO adsorption is plotted in Fig. 8(a). NO is located above the H site with a tilted structure and the N atom of the NO molecule is closer to the surface. A similar structure has been found for NO adsorption on InSe,[43] stanene[11] and antimonene.[52] After adsorption, the N–O bond length is elongated to 1.196 Å and the nearest atom-to-atom distance between the NO molecule and b-Bi is 2.773 Å. The adsorption energy for NO adsorption on b-Bi is −0.416 eV, which indicates a strong interaction. Furthermore, the ELF value between NO and b-Bi is 0.12 as shown in Fig. 7(b). Therefore, the NO molecule is bound to b-Bi by an ionic bond, similar to the case of SO_2 molecule adsorption on b-Bi.

The CDD for NO adsorbed on b-Bi is plotted in Fig. 8(b), showing that charge accumulation occurs on the N and O atoms while charge depletion appears on the N–O bond. The Bader charge calculation indicates that the NO molecule acts as an electron acceptor and gets 0.344 *e* from b-Bi. The band structures presented in Fig. 8(c) and Fig. S1(g) (ESI†) show that there are impurity states located inside the band gap and the values of the band gap are 0.58 eV (without SOC) and 0.57 eV (with SOC) without considering the impurity states. According to the PDOS analysis, the impurity states around the Fermi level are mainly attributed to the p orbitals of the N and O atoms and are slightly derived from the p orbital of the Bi atom. Due to the contributions of orbitals of the NO molecule near the Fermi level, the interaction between NO and b-Bi is strong and a

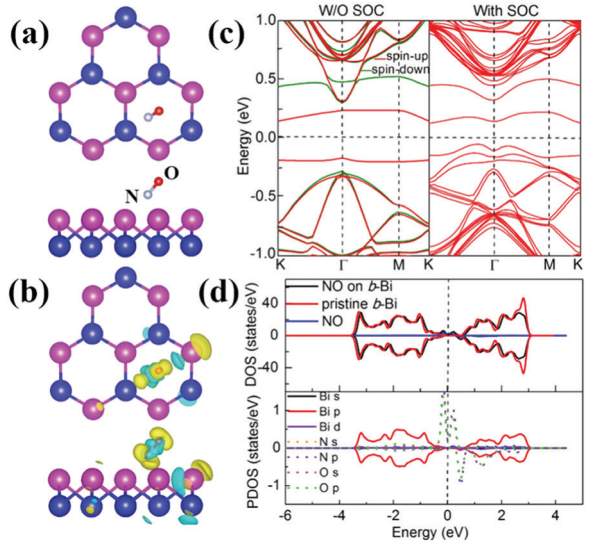

Fig. 8 NO adsorbed on b-Bi. (a) The most stable adsorption structure (top and side view). (b) Charge density difference with an isosurface value of 0.005 e Bohr^{-3}. (c) Band structures of b-Bi with NO adsorption (without and with SOC), and (d) the total (DOS) and partial (PDOS) electronic density of states (without SOC).

magnetic moment of 1.0 μ_B is induced in the NO adsorption system.

3.7 NO_2 adsorption

For the adsorption of the NO_2 molecule, the most stable structure is given in Fig. 9(a), where the N atom points away and the two O atoms point towards the b-Bi surface, being located at the V site. After adsorption, the N–O bond is elongated to 1.264 Å and the O–N–O angle is reduced to 113.8°. The adsorption energy of NO_2 on the b-Bi monolayer is −0.811 eV, which is the highest adsorption energy among all the investigated molecules. The nearest distance between the NO_2 molecule and the b-Bi monolayer is calculated to be 2.737 Å, which is larger than the Bi–O bond length of 2.14 Å.[49] Meanwhile, the ELF value for NO_2 (see Fig. 7(c)) is about 0.11, indicating the NO_2 molecule is bound to b-Bi by an ionic bond, similar to the case of NO_2 adsorption on antimonene[50] and an InN monolayer.[55]

The CDD is presented in Fig. 9(b), which shows obvious charge redistribution. Charge accumulation mainly appears on the N atom and partly on the O atoms while charge depletion is found on the O atoms and Bi atoms around the adsorbed NO_2 molecule. Bader charge analysis reveals that the NO_2 molecule obtains 0.663 *e* from b-Bi, which can lead to a significant decrease of electrons in the b-Bi monolayer and thus influence the conductivity of the system. From the band structures and PDOS shown in Fig. 9(c and d) and Fig. S1(h) (ESI†), we can see that the Fermi level shifts to the valence band, indicating a p-type doping effect. In addition, the O p and N p orbitals overlap with the new peak of the Bi p orbital between −0.3 eV and 0.1 eV, which demonstrates strong orbital hybridization and confirms the large charge transfer and high adsorption energy between NO_2 and b-Bi. As depicted in Fig. 9(c), the spin-up and spin-down states overlap with each other due to the loss of the magnetic moment of the NO_2 molecule, which is similar to the case of NO_2 molecule adsorption on germanene.[10]

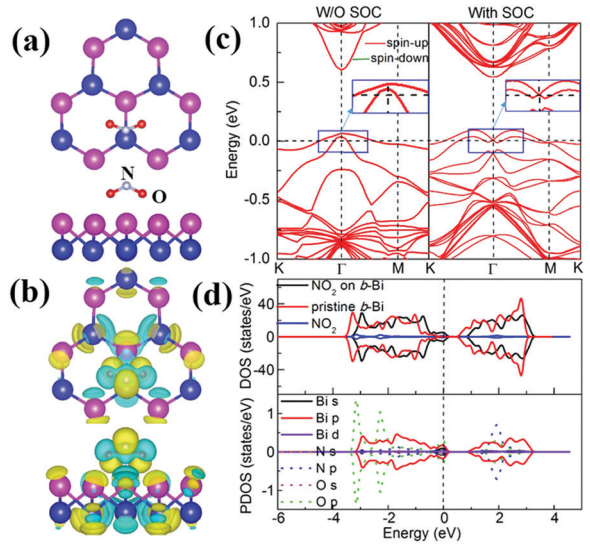

Fig. 9 NO_2 adsorbed on b-Bi. (a) The most stable adsorption structure (top and side view). (b) Charge density difference with an isosurface value of 0.005 e Bohr^{-3}. (c) Band structures of b-Bi with NO_2 adsorption (without and with SOC), and (d) the total (DOS) and partial (PDOS) electronic density of states (without SOC).

3.8 Transport properties

Due to the charge transfer between adsorbed molecules and b-Bi, the electron transport property of b-Bi is expected to be affected, which makes it possible for b-Bi to act as a gas sensor. To explicitly evaluate the influence of gas molecules on the transport properties of b-Bi, we calculated the quantum conductance of b-Bi with and without adsorption of four representative gases (NH_3, O_2, NO and NO_2). Due to the anisotropy of b-Bi, two models along the armchair and zigzag directions are shown in Fig. 10(a and b). It is clear that the conductance along

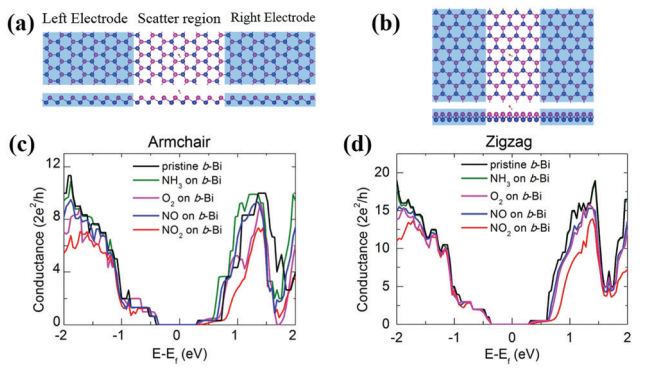

Fig. 10 Top: Schematic of two-probe systems of b-Bi along the (a) armchair and (b) zigzag directions with NO molecule adsorption. The upper and the lower panels are the top and side views of the device. Bottom: Computed quantum conductance of b-Bi with and without adsorption of NH_3, O_2, NO and NO_2 gas molecules along the (c) armchair and (d) zigzag directions.

the zigzag direction is higher in comparison to the armchair direction as presented in Fig. 10(c and d), which is also reflected in the *I–V* curves shown in Fig. S2 (ESI†). The current of zigzag pristine b-Bi under a bias of 1.1 V is 2.12 μA, while it is 0.39 μA for armchair pristine b-Bi. For the armchair direction, we can see that the conductance channels of pristine b-Bi increase and decrease after NH_3 adsorption in the conduction band region (Fig. 10(c)) and the current increases from 0.39 μA to 0.58 μA after NH_3 adsorption. The conductance is reduced after O_2 and NO adsorption, especially there is an obvious reduction of around 1.2 eV after O_2 adsorption, while the overall conductance is notably reduced after NO_2 adsorption, which confirms the largest electron transfer of NO_2 adsorption compared to other molecules. The reduction in conductance along the zigzag direction is similar to that of the armchair direction except for the NH_3 and O_2 adsorption. It is clear that the conductance and current have negligible change after NH_3 adsorption and the conductance has a slight reduction after O_2 adsorption along the armchair direction. Therefore, a b-Bi based device has great potential for detecting O_2, NO and NO_2 molecules based on the change of conductance after adsorption.

3.9 Diffusion energy barrier analysis

It is reported that the gas diffusion behavior has an important influence on the performance of a gas sensing device.[56,57] In order to investigate the gas diffusion energy barrier on b-Bi, we also chose four representative gases (NH_3, O_2, NO and NO_2) and explored diffusion between two neighboring stable sites along the armchair and zigzag directions as shown in Fig. S3 (ESI†). The diffusion energy barriers of NH_3, O_2, NO and NO_2 along the armchair direction are 0.157, 0.094, 0.108 and 0.109 eV, respectively, while the diffusion energy barriers of NH_3, O_2, NO and NO_2 along the zigzag direction are 0.077, 0.045, 0.059 and 0.088 eV, respectively. The results indicate that the diffusion along the zigzag direction is a little easier than that along the armchair direction. The transition states of NH_3, O_2, NO and NO_2 along the armchair direction correspond to the molecules adsorbed near the top of the upper Bi (T) sites, which indicates that the anisotropy of the diffusion energy barrier is mainly due to the buckled structure of b-Bi.

3.10 Work function (WF)

Previous studies have revealed that 2D materials exhibit interesting optical gas sensing properties.[58,59] To further investigate the potential use of b-Bi in an optical gas sensor, the work function (WF) of b-Bi with different adsorbed molecules is calculated and the results are shown in Fig. 11. The WF is defined as the minimum energy needed to move an electron from the interior of a solid material out of its surface, which can be defined as $\Phi = V_\infty - E_f$, where V_∞ and E_f represent the electrostatic potential of an electron at points far from the surface and at the Fermi level, respectively.[60] The WF of pristine b-Bi is 3.88 eV, which is smaller than that of pristine graphene (4.33 eV).[61] After the adsorption of small molecules, the values of the WF remain almost unchanged for the CO and H_2O adsorption configurations, whereas the WF increases to 4.15, 4.03, 3.97 and 4.27 eV after adsorption of O_2, SO_2, NO and NO_2 molecules, respectively, which indicates that the transfer of electrons to the vacuum level is hindered. In contrast, NH_3 adsorption causes the decrease of the WF to 3.82 eV. Therefore, the selective adsorption of small molecules can tune the WF of b-Bi, which makes b-Bi a promising candidate for optical gas sensors.

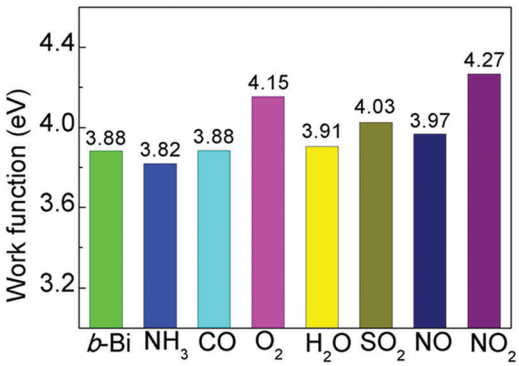

Fig. 11 The calculated work function for different molecules adsorbed on b-Bi as well as pristine b-Bi.

4 Conclusion

In summary, we have studied the adsorption configuration of CO, O_2, H_2O, NH_3, SO_2, NO, and NO_2 molecules on buckled bismuthene and their effects on the electronic, transport and optical properties using first-principles calculations. We find that all the studied molecules act as charge acceptors. The adsorption of SO_2, NO and NO_2 molecules on buckled bismuthene is a kind of chemisorption which is much stronger than the physisorption of CO, O_2, H_2O and NH_3 molecules. This is due to the large charge transfer and high adsorption energy and the contribution of the frontier orbitals of the SO_2, NO and NO_2 molecules near the Fermi level. Transport property calculations indicate that the quantum conductance of buckled bismuthene is obviously decreased after the adsorption of O_2, NO and NO_2. Also, the transport properties and the gas diffusion energy barriers show the anisotropy of buckled bismuthene along the armchair and zigzag directions. Moreover, the optical properties of buckled bismuthene can be tuned by the adsorption of different molecules. The change of the transport and optical properties of buckled bismuthene induced by the adsorption of gas molecules suggests that buckled bismuthene is a promising candidate for gas sensing materials.

Conflicts of interest

There are no conflicts to declare.

Acknowledgements

This work was supported by the National Natural Science Foundation of China under Grant No. 11575131, 11775163 and 11875208, and the Natural Science Foundation of Hubei

province under Grant No. 2016CFA080. The numerical calculations in this paper have been done on the supercomputing system in the Supercomputing Center of Wuhan University.

Notes and references

1 X. Liu, S. Cheng, H. Liu, S. Hu, D. Zhang and H. Ning, *Sensors*, 2012, **12**, 9635–9665.
2 A. Abbasi and J. J. Sardroodi, *New J. Chem.*, 2017, **41**, 12569–12580.
3 A. Abbasi and J. J. Sardroodi, *J. Appl. Phys.*, 2018, **124**, 165302.
4 X. Tang, A. Du and L. Kou, *Wiley Interdiscip. Rev.: Comput. Mol. Sci.*, 2018, **8**, e1361.
5 A. Abbasi and J. J. Sardroodi, *Appl. Surf. Sci.*, 2018, **442**, 368–381.
6 S. Varghese, S. Varghese, S. Swaminathan, K. Singh and V. Mittal, *Electronics*, 2015, **4**, 651–687.
7 A. Abbasi and J. J. Sardroodi, *Appl. Surf. Sci.*, 2019, **469**, 781–791.
8 S. Zhao, J. Xue and K. Wei, *Chem. Phys. Lett.*, 2014, **595–596**, 35–42.
9 S. K. Gupta, D. Singh, K. Rajput and Y. Sonvane, *RSC Adv.*, 2016, **6**, 102264–102271.
10 W. Xia, W. Hu, Z. Li and J. Yang, *Phys. Chem. Chem. Phys.*, 2014, **16**, 22495–22498.
11 X. Chen, C. Tan, Q. Yang, R. Meng, Q. Liang, M. Cai, S. Zhang and J. Jiang, *J. Phys. Chem. C*, 2016, **120**, 13987–13994.
12 L. Takahashi and K. Takahashi, *Phys. Chem. Chem. Phys.*, 2015, **17**, 21394–21396.
13 A. Abbasi and J. J. Sardroodi, *Phys. E*, 2019, **108**, 382–390.
14 C. Liu, C.-S. Liu and X. Yan, *Phys. Lett. A*, 2017, **381**, 1092–1096.
15 X.-P. Chen, L.-M. Wang, X. Sun, R.-S. Meng, J. Xiao, H.-Y. Ye and G.-Q. Zhang, *IEEE Electron Device Lett.*, 2017, **38**, 661–664.
16 P. Garg, I. Choudhuri and B. Pathak, *Phys. Chem. Chem. Phys.*, 2017, **19**, 31325–31334.
17 E. Aktürk, O. U. Aktürk and S. Ciraci, *Phys. Rev. B: Condens. Matter Mater. Phys.*, 2016, **94**, 014115.
18 S. Zhang, M. Xie, F. Li, Z. Yan, Y. Li, E. Kan, W. Liu, Z. Chen and H. Zeng, *Angew. Chem., Int. Ed.*, 2016, **55**, 1666–1669.
19 B. Radisavljevic, A. Radenovic, J. Brivio, V. Giacometti and A. Kis, *Nat. Nanotechnol.*, 2011, **6**, 147–150.
20 F. Yang, L. Miao, Z. F. Wang, M. Y. Yao, F. Zhu, Y. R. Song, M. X. Wang, J. P. Xu, A. V. Fedorov, Z. Sun, G. B. Zhang, C. Liu, F. Liu, D. Qian, C. L. Gao and J. F. Jia, *Phys. Rev. Lett.*, 2012, **109**, 016801.
21 F. Reis, G. Li, L. Dudy, M. Bauernfeind, S. Glass, W. Hanke, R. Thomale, J. Schäfer and R. Claessen, *Science*, 2017, **357**, 287–290.
22 Z. Liu, C. X. Liu, Y. S. Wu, W. H. Duan, F. Liu and J. Wu, *Phys. Rev. Lett.*, 2011, **107**, 136805.
23 M. Wada, S. Murakami, F. Freimuth and G. Bihlmayer, *Phys. Rev. B: Condens. Matter Mater. Phys.*, 2011, **83**, 121310.
24 L. Chen, Z. F. Wang and F. Liu, *Phys. Rev. B: Condens. Matter Mater. Phys.*, 2013, **87**, 235420.
25 L. Cheng, H. Liu, X. Tan, J. Zhang, J. Wei, H. Lv, J. Shi and X. Tang, *J. Phys. Chem. C*, 2013, **118**, 904–910.
26 Y. Kadioglu, S. B. Kilic, S. Demirci, O. U. Aktürk, E. Aktürk and S. Ciraci, *Phys. Rev. B: Condens. Matter Mater. Phys.*, 2017, **96**, 245424.
27 W. Oh, C. K. Rhee, J. W. Han and B. Shong, *J. Phys. Chem. C*, 2018, **122**, 23084–23090.
28 L. Chen, G. Cui, P. Zhang, X. Wang, H. Liu and D. Wang, *Phys. Chem. Chem. Phys.*, 2014, **16**, 17206–17212.
29 A. Abbasi, *Phys. E*, 2019, **108**, 34–43.
30 J. Sivek, H. Sahin, B. Partoens and F. M. Peeters, *Phys. Rev. B: Condens. Matter Mater. Phys.*, 2013, **87**, 085444.
31 A. Abbasi, *Synth. Met.*, 2019, **247**, 26–36.
32 G. Kresse and J. Furthmuller, *Comput. Mater. Sci.*, 1996, **6**, 15–50.
33 G. Kresse and D. Joubert, *Phys. Rev. B: Condens. Matter Mater. Phys.*, 1999, **59**, 1758–1775.
34 P. E. Blöchl, *Phys. Rev. B: Condens. Matter Mater. Phys.*, 1994, **50**, 17953–17979.
35 J. P. Perdew, K. Burke and M. Ernzerhof, *Phys. Rev. Lett.*, 1998, **77**, 3865–3868.
36 S. Grimme, *J. Comput. Chem.*, 2006, **27**, 1787–1799.
37 G. Henkelman and H. Jonsson, *J. Chem. Phys.*, 1999, **111**, 7010–7022.
38 G. Henkelman, B. P. Uberuaga and H. Jonsson, *J. Chem. Phys.*, 2000, **113**, 9901–9904.
39 G. Henkelman, A. Arnaldsson and H. Jónsson, *Comput. Mater. Sci.*, 2006, **36**, 354–360.
40 M. Brandbyge, J. L. Mozos, P. Ordejón, J. Taylor and K. Stokbro, *Phys. Rev. B: Condens. Matter Mater. Phys.*, 2002, **65**, 165401.
41 T. Nagao, J. Sadowski, M. Saito, S. Yaginuma, Y. Fujikawa, T. Kogure, T. Ohno, Y. Hasegawa, S. Hasegawa and T. Sakurai, *Phys. Rev. Lett.*, 2004, **93**, 105501.
42 M.-Y. Liu, Y. Huang, Q.-Y. Chen, Z.-Y. Li, C. Cao and Y. He, *RSC Adv.*, 2017, **7**, 39546–39555.
43 D. Ma, W. Ju, Y. Tang and Y. Chen, *Appl. Surf. Sci.*, 2017, **426**, 244–252.
44 D. R. Lide, *CRC handbook of chemistry and physics*, CRC Press, 2004.
45 O. Leenaerts, B. Partoens and F. M. Peeters, *Phys. Rev. B: Condens. Matter Mater. Phys.*, 2008, **77**, 125416.
46 M. Zhou, Y. H. Lu, Y. Q. Cai, C. Zhang and Y. P. Feng, *Nanotechnology*, 2011, **22**, 385502.
47 X.-Y. Liang, N. Ding, S.-P. Ng and C.-M. L. Wu, *Appl. Surf. Sci.*, 2017, **411**, 11–17.
48 Q. Yue, Z. Shao, S. Chang and J. Li, *Nanoscale Res. Lett.*, 2013, **8**, 425.
49 P. Pyykkö and M. Atsumi, *Chem. – Eur. J.*, 2009, **15**, 186–197.
50 R.-S. Meng, M. Cai, J.-K. Jiang, Q.-H. Liang, X. Sun, Q. Yang, C.-J. Tan and X.-P. Chen, *IEEE Electron Device Lett.*, 2017, **38**, 134–137.
51 Y. Cai, Q. Ke, G. Zhang and Y.-W. Zhang, *J. Phys. Chem. C*, 2015, **119**, 3102–3110.

52 A. A. Kistanov, Y. Cai, D. R. Kripalani, K. Zhou, S. V. Dmitriev and Y.-W. Zhang, *J. Mater. Chem. C*, 2018, **6**, 4308–4317.
53 A. D. Becke and K. E. Edgecombe, *J. Chem. Phys.*, 1990, **92**, 5397–5403.
54 T. Liu, Y. Chen, M. Zhang, L. Yuan, C. Zhang, J. Wang and J. Fan, *AIP Adv.*, 2017, **7**, 125007.
55 X. Sun, Q. Yang, R. Meng, C. Tan, Q. Liang, J. Jiang, H. Ye and X. Chen, *Appl. Surf. Sci.*, 2017, **404**, 291–299.
56 A. Abbasi and J. J. Sardroodi, *Environ. Sci.: Nano*, 2016, **3**, 1153–1164.
57 S. Killa, L. Cui, E. P. Murray and D. S. Mainardi, *Molecules*, 2013, **18**, 9901–9918.
58 Y. Liu, X. Dong and P. Chen, *Chem. Soc. Rev.*, 2012, **41**, 2283–2307.
59 L. Liu, Q. Yang, Z. Wang, H. Ye, X. Chen, X. Fan and G. Zhang, *Appl. Surf. Sci.*, 2018, **433**, 575–581.
60 G. S. Rao, T. Hussain, M. S. Islam, M. Sagynbaeva, D. Gupta, P. Panigrahi and R. Ahuja, *Nanotechnology*, 2016, **27**, 015502.
61 W. Geng, X. Zhao, H. Liu and X. Yao, *J. Phys. Chem. C*, 2013, **117**, 10536–10544.